npj | climate and atmospheric science

Article

Published in partnership with CECCR at King Abdulaziz University

https://doi.org/10.1038/s41612-024-00629-x

In-situ observations reveal weak hygroscopicity in the Southern Tibetan Plateau: implications for aerosol activation and indirect effects

Yuan Wang[1], Jiming Li[1] ✉, Fang Fang[1], Ping Zhang[1], Jianjun He[2], Mira L. Pöhlker[3], Silvia Henning[3], Chenguang Tang[1,4], Hailing Jia[5], Yang Wang[1], Bida Jian[1], Jinsen Shi[1] & Jianping Huang[1]

As a precursor process to cloud formation, aerosol activation over the Tibetan Plateau (TP) plays a pivotal role in regional cloud-precipitation and global climate. However, its characteristics remain unclear due to the absence of targeted observations in the TP. We conducted a ground in-situ aerosol-cloud-precipitation experiment in the southern TP (GACPE-STP), thereby unveiling the aerosol activation characteristics in this crucial region. Our findings reveal a weak aerosol activation capacity with low hygroscopicity (κ) values of less than 0.1 through multi-method κ measurements, contrasting starkly with the widely recommended κ value of 0.3 for continental regions. A κ parameterization is developed for predicting aerosol activation in this region, which can significantly reduce the overestimations of cloud droplet number concentration and hence aerosol indirect effects caused by using the recommended κ of 0.3. These findings address the unclear characteristics of aerosol activation in the TP region, contributing to the enhancement of regional cloud precipitation and global climate simulations.

Against the backdrop of the prevailing global climate change, the investigation of aerosol activation has assumed heightened importance. Serving as the pivotal link between aerosols and clouds, aerosol activation plays a pivotal role in the intricate interactions between aerosol and cloud[1,2], thereby exerting profound influences on precipitation[3,4], radiation[5–8], and the broader global climate system[9,10]. The latest assessment report from the Intergovernmental Panel on Climate Change (IPCC) underscores that aerosol-cloud interactions remain the most significant source of uncertainty in climate predictions[11]. Consequently, research endeavors focused on unraveling the intricacies of aerosol activation have emerged as a critical pathway to mitigate this uncertainty. The imperative to incorporate aerosol activation treatments into climate models has been accentuated, with the goal of refining predictions related to cloud properties and radiative forcing[12,13].

The theoretical basis of the aerosol activation process is rooted in Köhler theory[14], which enables the prediction of particle size growth for dry aerosols with known physical and chemical properties under specific environmental humidity conditions. However, its application to the natural atmosphere is not straightforward. This complexity arises from the intricate characterization of aerosol chemical properties in the Raoult term, necessitating input parameters like the van't Hoff factor, solute mass, molar mass, and others[14]. The diverse chemical composition of aerosols in the natural atmosphere further complicates obtaining these quantities. Consequently, early parameterizations of aerosol activation relied heavily on empirical fitting relationships between cloud condensation nuclei (CCN) number concentration (N_{CCN}) and the vapor supersaturation (SS), e.g., the classical power-law equation[15]. Petters and Kreidenweis[16] introduced a single parameter, aerosol hygroscopicity (κ), which relates the volume of water taken up by a particle to the water activity. This significantly improved the convenience of the Köhler theory, as it parameterizes the aerosol chemical properties in the Raoult term using a single variable. This advancement has led to a novel approach in aerosol activation parameterization, integrating

[1]Collaborative Innovation Center for Western Ecological Safety, College of Atmospheric Sciences, Lanzhou University, Lanzhou, China. [2]State Key Laboratory of Severe Weather and Key Laboratory of Atmospheric Chemistry of CMA, Chinese Academy of Meteorological Sciences, Beijing, China. [3]Experimental Aerosol and Cloud Microphysics Department, Leibniz Institute for Tropospheric Research, 04318 Leipzig, Germany. [4]Institute of Tropical and Marine Meteorology, China Meteorological Administration, Guangzhou, China. [5]SRON Netherlands Institute for Space Research, Leiden, the Netherlands. ✉e-mail: lijiming@lzu.edu.cn

the dry particle number size distribution (PNSD) with a parameterized κ to calculate N_{CCN} based on the κ-Köhler theory e.g.,[17–19]. This, in turn, motivated observational experiments on aerosol κ globally, aiming to capture the characteristics of κ in various regions, such as the Amazon rainforest[20,21], urban and suburban areas[22–25], rural locations[26,27], coastal regions[28,29], and high-altitude stations[30,31]. Summarizing various field experiments, Andreae and Rosenfeld[32] proposed κ values of 0.3 ± 0.1 and 0.7 ± 0.2 as representative for continental and marine aerosols, respectively. Subsequent studies have corroborated similar ranges of κ distributions and utilized this simple κ parameterization for activation calculations e.g.,[22,27,33–36].

The Tibetan Plateau (TP), considered the "Roof of the World", the "Asian Water Tower", and the "Heat Source Pump", wields a profound influence on regional precipitation and even global climate dynamics[37,38]. Given its distinctive geographic and climatic conditions, the exploration of aerosol, cloud, and precipitation processes in this region is crucial yet faces challenges. Especially, the κ and activation characteristics of aerosols in the TP region may deviate from the normal continental conditions, which, however, remain largely unexplored. To our knowledge, only Xu et al.[39] reported the $N_{CCN}(SS)$ measured at the eastern TP sites. The specific characteristics of κ in the TP region have yet to be documented. This knowledge gap does not stem from the insignificance of aerosol activation properties in the TP region but rather arises from observational challenges. Additionally, the unique topographical conditions, variability in aerosol sourcing, and the intricate interplay between topography and atmospheric flows collectively obscure a comprehensive understanding of the impacts on cloud and precipitation processes in the TP region[40–42]. Unraveling these complexities necessitates a foundation of high-precision, in-situ aerosol-cloud-precipitation microphysical observations. However, the formidable challenges linked to in-situ observations in the TP region hinder the implementation of such measurements. Consequently, current researches on aerosol-cloud-precipitation in this region mainly rely on satellite remote sensing and model simulations e.g.,[42–45], with scant reports of in-situ observational outcomes.

To advance our comprehension of aerosol-cloud-precipitation microphysical characteristics and their interactions within the Southern Tibetan Plateau (STP) region, we carried out the Ground in-situ Aerosol-Cloud-Precipitation Experiment on the STP (GACPE-STP) from August 17th to October 18th, 2023. As shown in Fig. 1, the research site (27.42 N, 88.90 E, 3136 m above sea level) is located in the mountainous region of Yadong County, China, in close proximity to the Indian border. The method section provides an overview of this endeavor. This study focuses on the characteristics of aerosol activation with three principal objectives: firstly, to elucidate the overall κ and activation characteristics of aerosols in the region; secondly, to access the appropriateness of the recommended continental κ value of 0.3[32] within the local context, evaluating its potential influence on predicting of cloud properties; and thirdly, to develop a κ parameterization for this region.

Results

Overall aerosol activation characteristics over STP

Figures 2a, b illustrate the temporal distribution of dry particle number size distribution (PNSD), total aerosol number concentration (N_a), aerosol median diameter (D_{median}), and N_{CCN} at various *SS* conditions during the observational period. The PNSD is predominantly characterized by an unimodal distribution, with a daily mean peak diameter varying in the range of 50 to 143 nm. The region exhibits relatively low N_a, with a mean value of 962 cm^{-3}. Daily mean N_a varies considerably, reaching a maximum of 1671 cm^{-3}, which is 4.3 times the minimum of 387 cm^{-3}. The daily-mean D_{median} also displays significant variations, with a mean of 93 nm and a maximum of 136 nm, representing 2.5 times the minimum of 54 nm. Additionally, a notable positive correlation exists between N_a and D_{median} (Supplementary Fig. 1), potentially linked to frequent cloud precipitation events during the observational period. Wet scavenging plays a pivotal role in reducing larger aerosol particles, simultaneously lowering N_a and D_{median}.

As *SS* increases, the critical dry activation diameter (D_c) decreases[16], leading to an increase in N_{CCN}. Unactivated particles significantly impact the CCN measurements, especially at low *SS* conditions[46,47]. At *SS* of 0.07%, the uncorrected daily-mean N_{CCN} is 68 cm^{-3}, corrected to only 24 cm^{-3}, with unactivated particles contributing to 65% of the measured N_{CCN}. At *SS* of 0.1% and 0.15%, the percentages decrease to 54 and 32%, respectively. Measurements at *SS* above 0.15% remain unaffected by unactivated particles. The region exhibits low N_{CCN} and activated fraction (*AF*, i.e., N_{CCN}/N_a) and the daily-mean values increase from 24 cm^{-3} to 483 cm^{-3} and 2 to 48%, respectively, as *SS* increases from 0.07% to 0.7%. The relatively low *AF* corresponds to the large D_c at each specific *SS* (Supplementary Fig. 2), implying weak κ, a characteristic explored in detail in the subsequent section. Figure 2c depicts that, within the same *SS* range, the N_{CCN} in the STP region is significantly lower than observations in rural e.g.,[26,27] and urban areas e.g.,[22,48], falling within the $N_{CCN}(SS)$ values observed in two Amazon tropical rainforest experiments[20,21]. The $N_{CCN}(SS)$ in the STP region is comparable with measurements recorded at the Qilian Observation and Research Station of Cryosphere and Ecologic Environment (LHG station) in the eastern TP region[39]. However, it stands distinctly lower than the $N_{CCN}(SS)$ obtained at the Waliguan station in the eastern TP region[39].

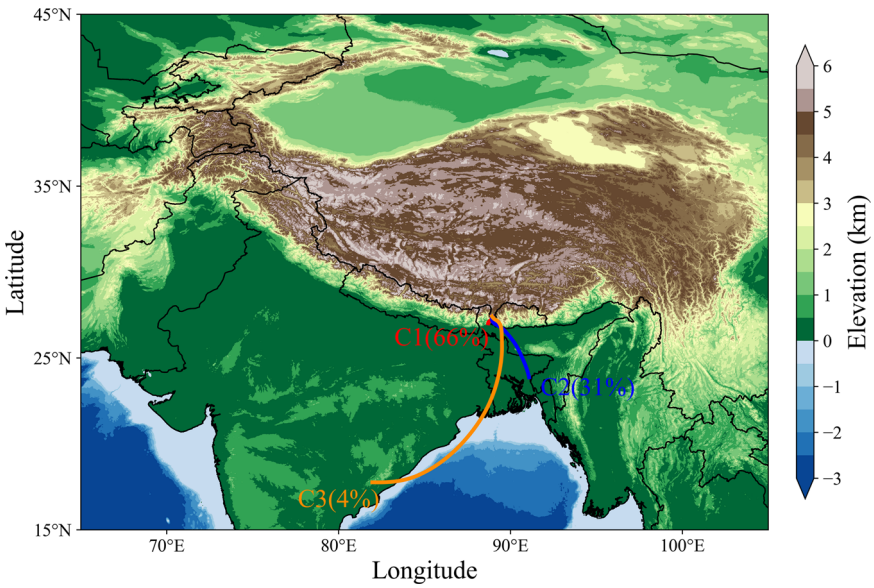

Fig. 1 | Geographic location of the GACPE-STP measurement site. Colored curves represent three clusters of three-day back trajectories generated using the HYSPLIT model.

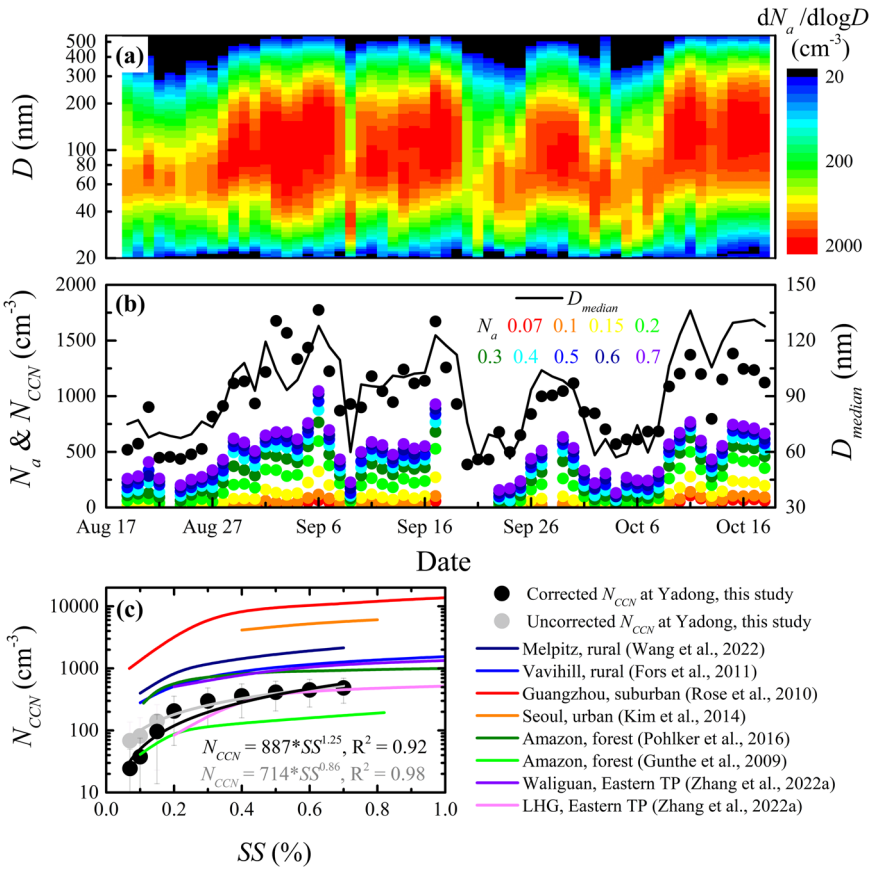

Fig. 2 | Time series of aerosol physical and activation properties and the CCN spectra. a Time series of daily-mean dry particle number size distribution and (**b**) dry aerosol number concentration (N_a), median diameter (D_{median}), and CCN number concentration (N_{CCN}) at various supersaturation (SS) conditions; **c** Relationships between N_{CCN} and SS at Yadong and other stations. The error bar represents one standard deviation.

Notably, these two stations, the LHG and Waliguan stations, represent the only reported locations with $N_{CCN}(SS)$ measurements in the TP regions.

Furthermore, the positive correlation between N_a and D_{median} increases the differences in N_{CCN} at different SS, reflected in an elevated k value of power-law fit[15]. The power-law fit for corrected N_{CCN} is represented as

$$N_{CCN} = 887SS^{1.25} \quad (1)$$

with R^2 of 0.92, where the k value of 1.25 is notably higher than the characteristic range of 0.4–0.9 summarized for continental regions by Seinfeld and Pandis[49]. The fitting results of the corrected $N_{CCN}(SS)$ using other functions are provided in Supplementary Fig. 3.

Various air masses exhibit noteworthy variations in aerosol activation characteristics. The prevailing air masses predominantly originated from the southern regions with relatively lower altitudes based on the simulations from HYSPLIT model, as shown in Fig. 1. According to the distance of air mass transport, it can be classified into three categories, as detailed in the Method Section. In Fig. 3, when air masses originate from local emissions and short-distance transport, designated as C1, the PNSD is characterized by the highest number concentration and largest particle size, with maximum values for N_a and D_{median} of 1091 cm^{-3} and 101 nm, respectively. Although κ is not the largest of the three clusters, the largest N_a and D_{median} contribute to the largest N_{CCN}. As the transport distance increases, the ability of aerosol activation weakens. In the scenario of air masses originating from long-distance transport, represented by C3, the PNSD becomes the lowest number concentration and smallest particle size, with the minimum values for N_a and D_{median} of 642 cm^{-3} and 61 nm, respectively. Furthermore, the κ is also the lowest among the three air mass clusters. The N_a, D_{median}, and κ are all the lowest, leading to the minimum N_{CCN} among the three air mass clusters. A plausible explanation for this phenomenon is that air masses transported over long distances undergo uplift due to topography, resulting in cloud and precipitation formation, which substantially depletes the effective CCN.

Weak hygroscopicity and its size-dependent

In Fig. 4a, the temporal evolution of κ, calculated through various methodologies during the observational period, is presented. Generally, κ within the STP region is observed to be notably low. The mean values of κ, calculated from N_{CCN} under a SS of 0.2% in column A ($\kappa_{ccn,0.2\%,A}$) and column B ($\kappa_{ccn,0.2\%,B}$) are 0.066 and 0.089, respectively. Additionally, the mean values of κ calculated from dry and wet particle median diameter, volume concentration, and scattering coefficient (κ_g, κ_v, and κ_f) are 0.054, 0.038, and 0.077, respectively. It is worth noting that κ_{ccn} corresponds to hygroscopicity under supersaturated conditions, while κ_g, κ_v, and κ_f all represent hygroscopicity at RH < 100% (more often, less than 90%). Additionally, κ_f is calculated under set RH cycles, while the RH corresponding to κ_g and κ_v varies with ambient RH. Previous studies on hygroscopicity have found that using HTDMA (humidity tandem differential mobility analyzer) to measure hygroscopicity at RH < 100% and CCNC to measure hygroscopicity at RH > 100% yields different results e.g.,[50,51]. Additionally, Zhao et al.[52] indicate that hygroscopicity varies with RH at RH < 100%. Therefore, the RH dependence of hygroscopicity could be a reason for the differences in hygroscopicity calculation results between these methods. Furthermore, the difference between κ_g and κ_v could be attributed to the neglect of curvature effects in the calculation of κ_v, while κ_g calculations do not neglect this term.

These κ values consistently remain below 0.1, much lower than the mean (0.3) and even lower bound (0.2) of the recommended mean κ value for continental regions[32]. The low value of κ is intricately associated with the surroundings at the observational site. Notably, vegetation in the STP regions surrounding by forests and meadows is recognized for emitting volatile organic compounds (VOCs)[53]. The secondary organic aerosols (SOA) formed as precursors from VOCs exhibit either negligible or weak hygroscopicity. Examples include SOA formed as precursors from α-pinene

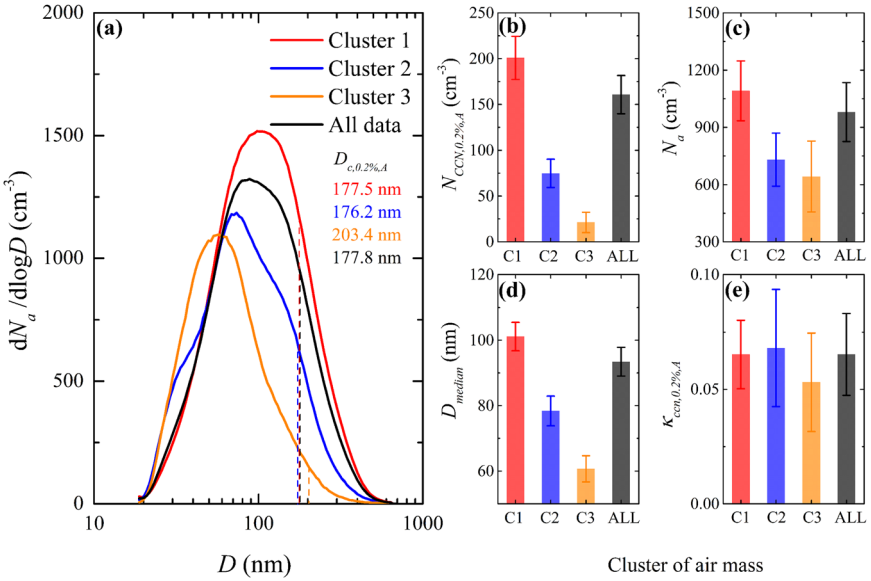

Fig. 3 | Physical and activation properties of aerosols from different air mass clusters. a The mean particle number size distribution (dN_a/$dlogD$), **b** CCN number concentration at a supersaturation of 0.2% in column A ($N_{CCN,0.2\%,A}$), **c** total aerosol number concentration within a diameter ranging from 18.8 to 685.4 nm (N_a), **d** median diameter of dry particles (D_{median}), and (**e**) hygroscopicity calculated by $N_{CCN,0.2\%,A}$ ($\kappa_{ccn,0.2\%,A}$). The error bar represents one standard deviation. The trajectories of the air mass clusters are in Fig. 1.

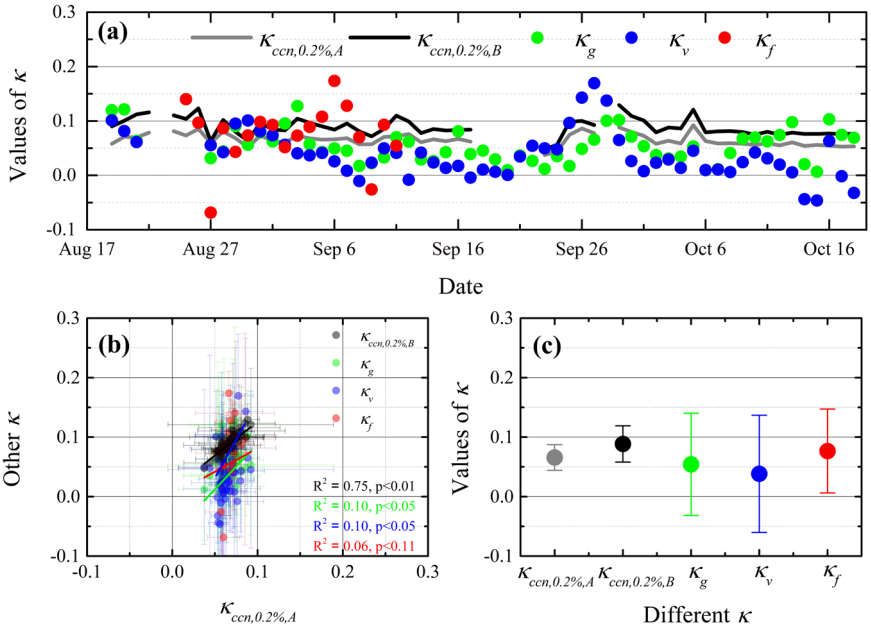

Fig. 4 | Time series of various aerosol hygroscopicity (κ) values and their comparisons. a Time series of daily-mean κ values derived by N_{CCN} in column A at *SS* of 0.2% ($\kappa_{ccn,0.2\%,A}$), N_{CCN} in column B at *SS* of 0.2% ($\kappa_{ccn,0.2\%,B}$), dry and wet median diameter (κ_g), volume concentration (κ_v), and scattering coefficient of aerosol (κ_f); **b** Relationships among the five κ values; **c** Statistical mean value and one standard deviation of the five κ. The error bar represents one standard deviation.

and β-pinene, both exhibiting a reported κ value of 0.022[54]. Furthermore, inhabitants of the STP region adhere to distinctive lifestyles, utilizing domestic fuels that diverge from those commonly found in other regions of China. The combustion of biofuels such as yak dung, WeiSang mixture fuels, and powdery Tibetan incense, characterized by lower combustion efficiencies, leads to significant emissions of CO and organic aerosols[55]. Organic aerosols and black carbon, as the predominant components stemming from biomass burning activities, collectively contribute to more than 69.1−85.7% of the total PM_1 mass at four sites in the southern and central TP[39]. These observations lend support to the measured low κ in the conducted experiment.

The daily-mean κ_{ccn} displays a reduced temporal fluctuation when compared to κ_g, κ_v, and κ_f. This phenomenon can be ascribed to the relatively low aerosol loading at the measurement site. The calculation of κ, relying on measurements of both dry and wet aerosol properties (i.e., κ_g, κ_v, and κ_f), is notably influenced by instrumental bias due to the low aerosol loading, resulting in substantial fluctuations and occasional negative values. This effect further diminishes the correlation between the κ values calculated by different methods, as illustrated in Fig. 4b. The temporal trends of $\kappa_{ccn,0.2\%,A}$ and $\kappa_{ccn,0.2\%,B}$ exhibit similarity with a strong correlation. However, the absolute mean value of $\kappa_{ccn,0.2\%,B}$ is elevated by 0.023 compared to $\kappa_{ccn,0.2\%,A}$, representing a 35% relative increase. This discrepancy is primarily attributed to the N_{CCN} in column B being 24% higher than that in column A at *SS* of 0.2%.

Size-dependent κ can be calculated based on N_{CCN} (*SS*) and dry PNSD. Figure 5 presents the relationships between κ and dry particle diameter (D) observed in this study, along with measurements from various regions. It is crucial to emphasize that under low *SS* conditions, the presence of unactivated particles in CCN measurements markedly increases the uncorrected N_{CCN}, leading to a decrease in D_c and an increase in κ[16]. Consequently, a monotonically increasing relationship between κ and D is obtained. However, upon excluding unactivated particles, the authentic relationship between κ, calculated using corrected N_{CCN}, and D conforms to a Gaussian distribution that κ initially increases with D and subsequently decreases as D

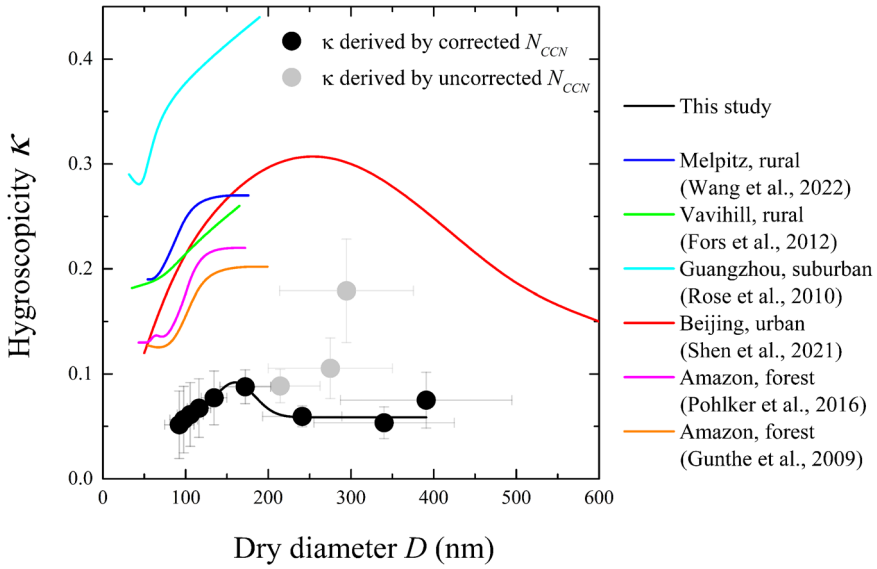

Fig. 5 | Relationships between the aerosol hygroscopicity (κ) and dry diameter (*D*). The error bar represents one standard deviation. The black line is the Gaussian fit of the κ vs. *D* pairs observed in GACPE-STP, while the other lines represent the κ vs. *D* relationships observed at various stations.

increases. The fitting results are expressed as follows:

$$\kappa_{ccn} = 0.059 + 0.033 \exp\left[-2\left(\frac{D - 159.8}{47.87}\right)^2\right] \quad (2)$$

with R^2 of 0.74. The peak of the fitting curve occurs at *D* of 159.8 nm, with a peak κ of 0.092. The κ(*D*) values in the STP region are consistently lower than those measured in rainforests e.g.,[20,21], rural areas e.g.,[26,27], and urban environments e.g.,[22,56]. This observation signifies a prevailing trend of low κ values for different particle sizes in the STP region.

Furthermore, owing to the *SS* cycling established in this experiment spanning from 0.07% to 0.7% and the low κ of the region, the mean D_c measured in this study is 391 nm at *SS* of 0.07%, decreasing to 92 nm at *SS* of 0.7%. Consequently, this experiment provides a relationship between κ and *D* in the mean *D* range of 92 to 391 nm. Notably, this range is more extensive than those obtained in previous CCN and HTDMA measurements, particularly in the larger particle size range. For instance, in Wang et al.[27], a monotonically increasing relationship between κ and *D* was observed within the range of 40 to 200 nm. Additionally, in other studies e.g.,[20–22,25,26], a consistent monotonically increasing relationship between κ and *D* was reported, but the *D* ranges in these studies were confined to 30 to 250 nm. Shen et al.[56], employing an HTDMA to explore urban size-resolved κ across an extended size range of 50 to 600 nm, highlighted that κ initially increases with *D* and then decreases, deviating from a monotonically increasing trend. This behavior is ascribed to the lag time for different sizes to respond to the evolution of pollution. Concerning the κ-*D* relationship, the findings of Shen et al.[56] align with our observations. Nevertheless, the mechanisms governing the variation of κ with *D* in the STP region warrant further investigation, particularly through the inclusion of size-resolved aerosol chemical composition.

Implications for aerosol activation and the aerosol indirect effects

Accurate prediction of cloud droplet number concentration (N_c) in weather and climate models hinges upon a comprehensive understanding of aerosol activation characteristics[12]. The approach based on the κ-Köhler theory utilizes parameterized κ and dry PNSD to predict N_{CCN}, representing a significant development in aerosol activation parameterization. Its predictive efficacy notably surpasses that of empirical fits of N_{CCN} and *SS*[27]. Consequently, an imprecise depiction of κ can introduce biases in predicting N_{CCN} and N_c. When concerning aerosol activation and cloud formation, κ_{ccn} emerges as the preferable parameter for characterizing κ, in contrast to κ_f, κ_g and κ_v. This preference arises because κ_{ccn} embodies hygroscopicity under supersaturated conditions, reflecting the conditions under which aerosol activation and cloud formation occur. The relationship between κ_{ccn} and *D*, derived from this observation and expressed in Eq. 2, can serve as a parameterization of κ for predicting N_{CCN} in the STP region.

We evaluate deviations of calculating N_{CCN} arising from employing κ of 0.3 and incorporating the fitted relationship κ(*D*) as outlined in Eq. 2. Figure 6 illustrates the relationship between measured N_{CCN} and predicted N_{CCN} under various *SS* conditions. Setting κ equal to 0.3 significantly overestimates N_{CCN} in the STP region, particularly at low *SS* and low N_{CCN} conditions, where the overestimation of N_{CCN} can surpass one order of magnitude. The utilization of κ parameterized by Eq. 2 effectively mitigates this overestimation, resulting in improved predictions for N_{CCN} in the STP region. It is noteworthy that, despite κ being set at 0.3 resulting in a significant overestimation of N_{CCN}, there is a distinct positive correlation between the predicted and measured N_{CCN}. This correlation is attributed to the use of measured dry PNSD in N_{CCN} calculations, where particle size plays a more dominant role than chemical composition in predicting N_{CCN}[57]. Figure 7a quantifies the measured and predicted mean N_{CCN} under different *SS* conditions, which is then utilized to calculate the relative prediction biases shown in Fig. 7b. When employing $\kappa = 0.3$ to predict N_{CCN}, a significant overestimation occurs, with a minimum bias of 77% at *SS* of 0.7% and a maximum bias up to 426% at *SS* of 0.1%. In contrast, using the κ(*D*) parameterization from Eq. 2 results in a shift in the mean N_{CCN} prediction bias from −51 to 26% as *SS* increases from 0.07% to 0.7%, demonstrating better performance than assuming $\kappa = 0.3$. Therefore, the recommended $\kappa = 0.3$ for the continental regions[32] does not hold for the STP region.

The discrepancy in predicting N_{CCN} directly translates to a forecast bias in N_c, subsequently impacting predictions of cloud radiative characteristics and precipitation processes, thereby influencing the assessment of aerosol indirect effects (AIEs). Lastly, we provide a brief evaluation of the impact of the two κ parameterization methods on AIEs. Cloud optical thickness (τ_c) can be approximately expressed as a function of cloud liquid water path (*LWP*) and cloud droplet effective radius (r_e) according to Stephens[58]:

$$\tau_c \approx \frac{3LWP}{2r_e} \quad (3)$$

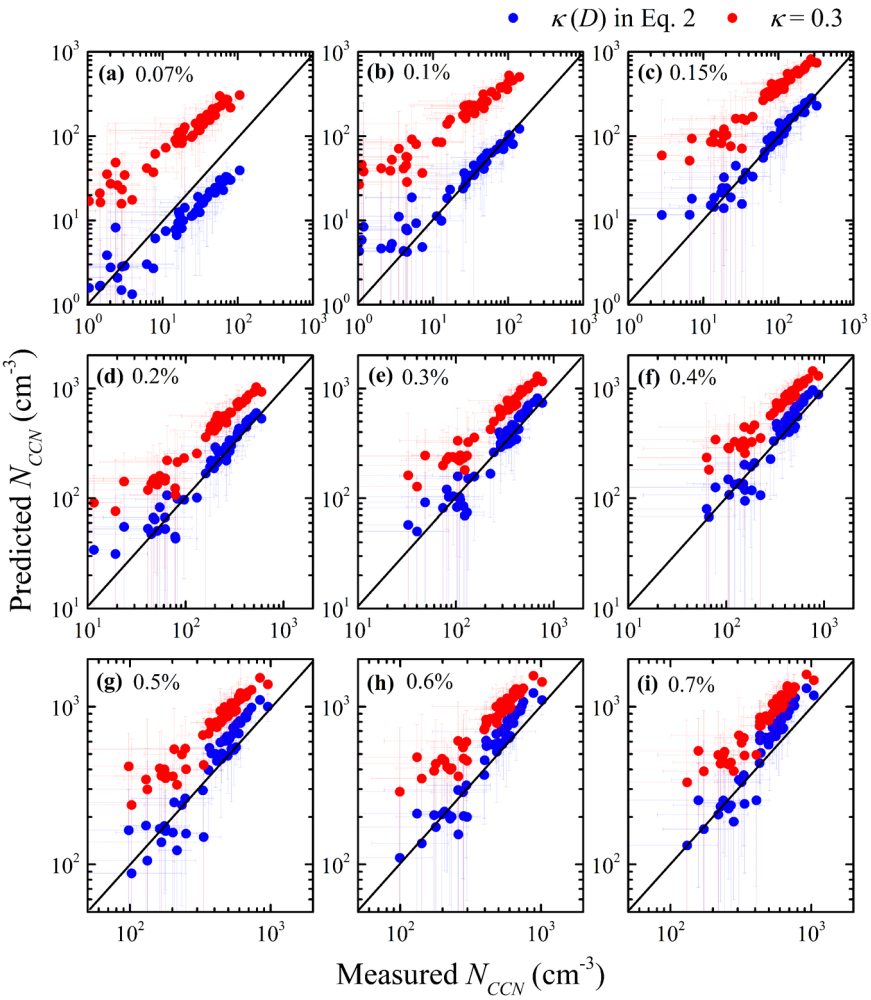

Fig. 6 | Predicted vs. measured CCN number concentrations (N_{CCN}). **a**–**i** represent different supersaturation (*SS*) conditions (0.07% to 0.7%). Predictions are based on the κ-Köhler model approach using two types of effective hygroscopicity parameters (κ): κ vs. particle diameter (D) relationship in Eq. 2 (blue points) and constant value of $\kappa = 0.3$ (red points).

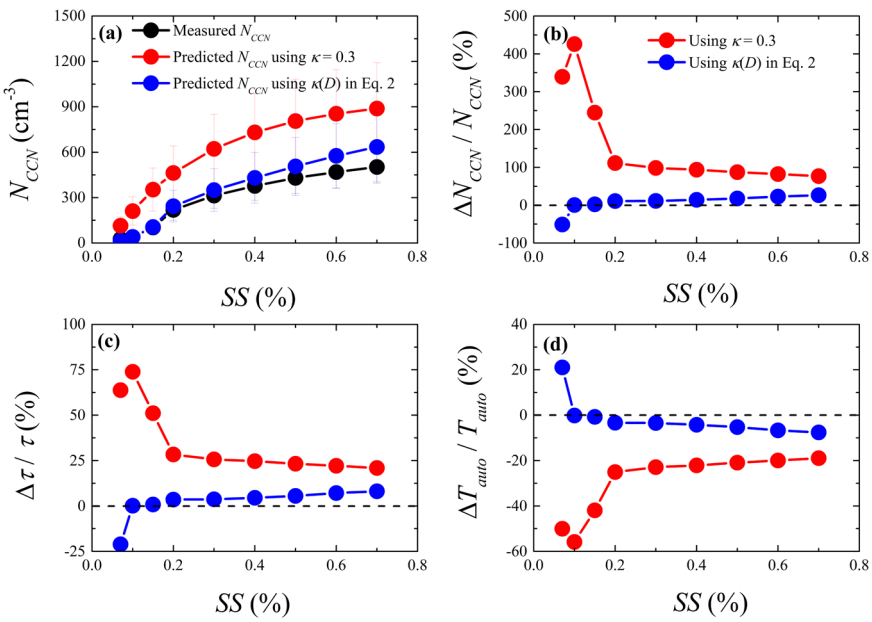

Fig. 7 | The effect of weak hygroscopicity on aerosol activation and indirect effects. **a** Measured and predicted CCN number concentration (N_{CCN}) at different supersaturation (*SS*) conditions; **b** Relative deviation between predicted and measured N_{CCN}; **c** Relative deviation to cloud optical thickness (τ); **d** Relative deviation to the threshold function of the cloud-to-rain transition (T_{auto}).

where r_e is proportional to volume-mean radius (r_v):

$$r_e = \beta r_v = \beta\left(\frac{3LWC}{4\pi\rho_w N_c}\right)^{1/3} \quad (4)$$

Here, LWC represents liquid water content, β is the ratio of r_e to r_v, and is a function of relative dispersion of cloud droplet spectrum[59]. When neglecting dispersion effects, β can be assumed as a constant, e.g., $\beta = 1.1$ used in Quass et al.[60]. Additionally, N_c impacts the efficiency of cloud-rain autoconversion, thereby influencing the collision-coalescence and

precipitation process. The formulation of the autoconversion threshold function (T_{auto}) is defined by Liu et al.[61]:

$$T_{auto} = \left[\frac{\int_{r_c}^{\infty} r^6 n(r)dr}{\int_0^{\infty} r^6 n(r)dr}\right]\left[\frac{\int_{r_c}^{\infty} r^3 n(r)dr}{\int_0^{\infty} r^3 n(r)dr}\right] \quad (5)$$

where r is the cloud droplet radius, $n(r)$ is the cloud droplet spectrum, and we utilize the $n(r)$ observed by a fog monitor (FM-120, DMT Inc.) during a cloud event with drizzles on 2023/08/26 as an illustrative example for calculating T_{auto}. The critical radius for autoconversion (r_c) is determined by an analytical expression based on N_c and LWC[62]:

$$r_c \approx 4.09 \times 10^{-4} \beta_{con}^{1/6} \frac{N_c^{1/6}}{LWC^{1/3}} \quad (6)$$

where β_{con} is an empirical coefficient with a value of $1.15*10^{23}\,s^{-1}$. The LWC can be derived as:

$$LWC = \frac{4\pi\rho_w}{3}\int_0^{\infty} r^3 n(r)dr \quad (7)$$

where ρ_w represents the liquid water density. T_{auto} ranges from 0 to 1, with higher values indicating an increased probability of collision-coalescence occurring in clouds.

In the assumption of constant LWC and LWP, an overestimation of N_c results in an underestimation of r_e, ultimately leading to an overestimation of τ_c. As shown in Fig. 7c, using $\kappa = 0.3$ causes an overestimation of τ_c ranging from 21 to 74% within the SS range of 0.07% to 0.7%. In contrast, when employing the $\kappa(D)$ parameterization from Eq.2, τ_c is underestimated by 21% at SS of 0.07% and overestimated by less than 8% within the SS range of 0.1% to 0.7%. Additionally, the overestimation of N_c leads to an overestimation of r_e, resulting in an underestimation of T_{auto}. As shown in Fig. 7d, using $\kappa = 0.3$ results in an underestimation of T_{auto} ranging from −19% to −56% within the SS range of 0.07% to 0.7%. Conversely, employing the $\kappa(D)$ parameterization from Eq. 2 leads to an overestimation of T_{auto} by 21% at SS of 0.07% and an underestimation by less than 8% within the SS range of 0.1% to 0.7%. Hence, concerning clouds within the STP region, the employment of $\kappa = 0.3$ amplifies the Twomey effect and prolongs cloud lifetime through the attenuation of the collision-coalescence process. Conversely, when utilizing the $\kappa(D)$ parameterization from Eq. 2, the predictive bias for AIEs is significantly reduced. It is worth emphasizing that, in contrast to high SS conditions, the deviations in predicting τ_c and T_{auto} are more prominent when $\kappa = 0.3$ is employed under low SS conditions (e.g., $SS < 0.2\%$). This underscores a more substantial influence on shallow clouds and fogs with relatively low values of SS e.g.,[63–65].

Discussions

As the "Asian Water Tower", clouds in the Tibetan Plateau have a substantial impact on regional water resource distribution and the global climate[37,38]. As the important physical process of cloud formation, the characteristics of aerosol activation significantly influence the microphysical properties of clouds in the TP region. However, current research on aerosol activation in the TP region is nearly non-existent, with scarcely documented studies, contributing to deviations in cloud and precipitation simulations and climate prediction. As part of the Second Tibetan Plateau Scientific Expedition and Research Program, we conducted a comprehensive in-situ aerosol-cloud-precipitation experiment in the STP region. This study focuses on the observational results of aerosol activation characteristics, revealing the aerosol hygroscopicity and activation characteristics in the STP region. The specific results are summarized as follows.

The overall aerosol activation capacity in this region is weak, manifested by low N_{CCN} and AF, along with weak hygroscopicity. In the SS ranges of 0.07% to 0.7%, the mean N_{CCN} and AF spans from 24 to 483 cm^{-3} and 2 to 48%, respectively. Aerosol hygroscopicity, calculated through various measurements, including amalgamation of $N_{CCN}(SS)$ with dry PNSD, as well as the median particle size, volume concentration, and scattering coefficient of dry and wet aerosols, all indicate weak hygroscopicity with mean values below 0.1. This phenomenon may be attributed to the distinctive underlying surface and fuel usage practices among residents in the STP region[55]. Air masses in this region mainly originate from local emissions and the transport from its southern lower-altitude regions. With an increase in air mass transport distance, the proportion of air masses decreases, and the aerosol activation capacity weakens due to the effective CCN being depleted in the process of cloud and precipitation formation during the ascent along the terrain.

The $\kappa(D)$ was derived through the integration of $N_{CCN}(SS)$ and dry PNSD, revealing a non-monotonic correlation between particle size and κ. As particle size increases, κ initially rises and subsequently decreases, reaching its peak at a diameter of 159.8 nm. The $\kappa(D)$ relationship follows a Gaussian distribution, with fitting results suitable for κ parameterization to model aerosol activation. Utilizing this $\kappa(D)$ parameterization induces a shift in the mean N_{CCN} prediction bias from −51 to 26% as SS increases from 0.07% to 0.7%. Conversely, employing the recommended κ value of 0.3 for continental regions[32] to predict cloud droplet activation in the TP region could result in an overestimation of N_{CCN} and N_c by more than four times, especially at the SS of 0.1%. This could further lead to a 74% overestimation of cloud optical thickness and a 56% underestimation of the cloud-rain autoconversion threshold function, suggesting a substantial overestimation of the aerosol indirect effects. These discrepancies can be effectively mitigated by adopting the $\kappa(D)$ parameterization proposed in this study.

These findings reveal the characteristics of aerosol activation in the STP region, contributing to a refined comprehension of cloud formation in the TP region and an improvement of regional cloud precipitation and global climate simulations. Although these are in-situ observational results from a single station in the STP region, it is notable that aerosol chemical composition measurements conducted at various sites in the STP region consistently indicate a high proportion of organic aerosol and black carbon[39]. This implies that weak hygroscopicity is likely a prevalent feature in the STP region. Nevertheless, advocating for more in-situ experiments with a focus on aerosol activation characteristics, including the measurements of aerosol hygroscopicity, CCN, and ice nuclei, in the TP region is advisable. Such endeavors would contribute to a more comprehensive understanding of aerosol activation capacity in the region, ultimately refining the accuracy of simulations related to plateau cloud-precipitation and climate. Furthermore, the $\kappa(D)$ parameterization proposed in this study requires validation through a more extensive and prolonged collection of hygroscopicity measurements from TP region and remains to be applied into models to evaluate its predictive performance on aerosol activation.

Methods

Experiment and data

As part of the Second Tibetan Plateau Scientific Expedition and Research Program, the primary objective of GACPE-STP is to conduct observations of aerosols, clouds, and precipitation in the TP region. The visual representations of the experimental square cabin and the instruments employed in this experiment are provided in Supplementary Fig. 4 and Supplementary Table 1. Positioned approximately 10 kilometers from residential areas, the site is enveloped by forests and meadows. The aerosol optical properties at this location have been reported in Tian et al.[66]. The goals of GACPE-STP encompass two key aspects. Firstly, it aims to address the deficiency in microphysical observations of aerosols, clouds, and precipitation in the plateau region, while also seeking to elucidate the mechanisms through which aerosols activate and lead to cloud formation and subsequent precipitation. Secondly, it endeavors to quantify aerosol-cloud interactions in the plateau region and reduce the predictive uncertainties associated with the aerosol indirect effect in this specific area.

The focus of this study revolves around the characteristics of aerosol activation, which is largely unexplored in the TP region. Supplementary Figure 5 provides a schematic diagram illustrating the experimental setup

used for measuring aerosol activation. Two scanning mobility particle sizers (SMPS, model 3938L50; TSI Inc.) were employed to assess PNSD under both dry and ambient relative humidity (*RH*) conditions. The measured diameter ranged from 18.8 to 685.4 nm, divided into 101 bins, and PNSD data was collected at 2-minute intervals. It is worth noting that we installed a water storage bottle before the wet SMPS inlet to prevent cloud droplets from blocking the inlet of wet SMPS. A CCN counter equipped with double cloud columns (CCNC, model 200; DMT Inc.) was utilized to determine the N_{CCN} at varying *SS* conditions. A constant *SS* of 0.2% was maintained in column A. In column B, a total of nine distinct *SS* conditions were cycled, i.e., 0.07%, 0.1%, 0.15%, 0.2%, 0.3%, 0.4%, 0.5%, 0.6%, and 0.7%. Among these *SS* conditions, the measurement was set at *SS* = 0.07% for a duration of 15 min, while the others were each set at 5 min. Only CCN data with a temperature-stabilized state are used for analysis, comprising approximately 70% of the total CCN dataset of column B. To simultaneously measure the dry scattering coefficient ($\sigma_{sc,dry}$) and the scattering coefficient at a specific RH ($\sigma_{sc,wet}$), an improved humidified nephelometer system (PB-FRH100; BMET Inc.) was employed. The RH cycle set for the wet nephelometer ranges from 70 to 91%, with a 25-minute cycle period. Its operating principle, hardware configuration, and the uncertainty of observation data were described in Kuang et al.[67] and Zhao et al.[68].

The instruments were meticulously calibrated throughout the experiment. The CCNC was calibrated following the procedures as outlined in Rose et al.[69]. The *SS* calibration curves for column A and B in CCNC are in Supplementary Fig. 6. The PB-FRH100 was subjected to cleaning and calibration procedures. Data quality was initially assessed by scrutinizing the consistency of measurements acquired from diverse instruments, and the results are presented in Supplementary Fig. 7. The N_a measured by the two SMPS exhibited a high level of concordance, with an average deviation of a mere 7%. Meanwhile, the N_{CCN} flowing through the two cloud columns at *SS* of 0.2% within the CCNC demonstrated a robust correlation. However, on average, N_{CCN} in column A was 24% lower than that in column B. Although this deviation is well within the expected range for the instrument, it causes a 35% difference in κ calculation. Moreover, $\sigma_{sc,dry}$ and $\sigma_{sc,wet}$ at 525 nm recorded by the two nephelometers in the PB-FRH100 exhibited a strong and consistent correlation. An increase in humidity had a minor effect on N_a but a significant influence on aerosol volume concentration (V_a) and σ_{sc} due to the hygroscopic growth of aerosols. Therefore, it is reasonable to observe higher $\sigma_{sc,wet}$ compared to $\sigma_{sc,dry}$. Furthermore, significant correlations were observed between dry N_a and N_{CCN} in column A, as well as between dry N_a and $\sigma_{sc,dry}$, affirming the expected relationship that increased N_a correspondingly yields higher N_{CCN} and enhanced scattering effects. As such, these results affirm the relatively high quality of the data.

Methods for calculating κ

Based on the observations provided by these instruments, we applied four distinct methods to calculate aerosol κ, each offering a unique perspective. The κ derived from these diverse methods can undergo cross-validation. The schematic diagram for the four methods is provided in Supplementary Fig. 8. The four methods can be categorized into two groups: the first involves the calculation of κ through the integration of $N_{CCN}(SS)$ and dry PNSD, while the second pertains to the determination of κ based on the concurrent measurements of both dry and wet aerosol properties. Details of the algorithms are as follows.

κ derived from N_{CCN} (*SS*) and dry PNSD

Particle size matters more than chemistry for aerosol activation ability[57] and the humidity requirement for activation decreases with increasing dry particle size[14,16]. Affected by aerosol mixing, the *AF* exhibits a gradual increase with dry particle diameter, following a sigmoidal pattern rather than an abrupt step function. The D_c is subsequently defined as the dry particle size at which 50% of the dry particles activate at a specified *SS*.

In the case of assuming internal mixing, D_c can be determined by integrating the dry PNSD from larger to smaller particle sizes until it matches the N_{CCN} (*SS*) as

$$N_{CCN,SS} = \int_{D_{c,SS}}^{D_{\max}} PNSD\,(D)\,dD \tag{8}$$

where D is dry particle diameter, D_{max} represents the maximum D, which, in this context, is 685 nm as determined by the SMPS. Linear interpolation was employed in cases where D_c did not align with the lower or upper diameters of each bin in the PNSD.

Then hygroscopicity (κ_{ccn}) can be determined by taking the derivative of the κ-Köhler equation[16] with respect to D_c and *SS*:

$$\kappa_{ccn} = \frac{4A^3}{27D_c^{\,3}\ln^2\left(1 + SS/100\right)} \tag{9}$$

where A can be considered a function of the absolute temperature. In this study, we assumed $\sigma_{s/a}$ to be that of pure water, specifically 0.0728 Nm^{-2}. Ongoing debates surround the significance of $\sigma_{s/a}$ variations and the associated bulk/surface partitioning in the activation of aerosols[70] which is not focused on in this study. Various *SS* values were set within column B in the CCNC, yielding $N_{CCN}(SS)$. This $N_{CCN}(SS)$ data was subsequently utilized in Eq. 8 to derive $D_c(SS)$, which was then employed in Eq. 9 to calculate the κ_{ccn} at each $D_c(SS)$.

This algorithm determines D_c and κ_{ccn} from collocated polydisperse CCN and dry PNSD measurements, similar methodology that has been employed in prior studies e.g.,[23,31,71]. The limitations of this algorithm are primarily associated with the inherent bias in N_a and N_{CCN} measurements obtained from the SMPS and CCNC. To mitigate this uncertainty, one solution is to employ a monodisperse CCN measurement system[27]. Nevertheless, due to the low background N_a at the experimental site, the N_a for specific particle sizes, as isolated using the monodisperse differential mobility analyzer (DMA), and the corresponding N_{CCN} often fall below 1 cm^{-3}, introducing substantial measurement bias. As such, the polydisperse CCN measurements were chosen for both columns A and B of CCNC within this experiment. Additionally, it's worth noting that Eq. 9 is derived from an approximation of the κ-Köhler equation, and it may introduce a slight bias in the calculation of κ_{ccn} when dealing with particles that are less-hygroscopic[16].

Furthermore, CCN measurements may include unactivated particles that are incorrectly classified as CCN[46,47], resulting in an overestimation of N_{CCN}, especially at low *SS* conditions. Wang et al.[46] introduced an approach based on the inverse relationship between the critical wet activation diameter of droplets ($D_{c,wet}$) and the critical *SS* to identify unactivated particles and correct the CCN measurements. Tao et al.[72] further considered the impact of kinetic limitations and improved the determination of $D_{c,wet}$ using a validated kinetic model[73]. In this study, we applied the $D_{c,wet}$ from Tao et al.[72] with assuming an accommodation coefficient of water vapor of 0.2 to rectify the N_{CCN} measurements at low *SS* conditions.

κ derived from dry and wet aerosol properties

The impact of aerosol hygroscopic growth is noticeable in the increase of wet particle sizes, resulting in higher V_a and σ_{sc}. The hygroscopic growth factor for particle diameter ($g(RH)$) is defined as the ratio of wet particle diameter at a specific RH to the corresponding dry diameter, expressed as:

$$g(RH) = \frac{D(RH)}{D(RH_{dry})} \tag{10}$$

The κ-Köhler equation, expressed in terms of g, is given in Eq. 11 below:

$$\frac{RH}{100} = \frac{g^3 - 1}{g^3 - (1 - \kappa_g)} \exp\left(\frac{A}{D(RH)}\right) \tag{11}$$

Given that RH at the dry condition (RH_{dry}) is not zero in dry SMPS, κ_g can be derived as

$$\kappa_g = (1-g^3) \Big/ \left[\frac{g^3 RH_{dry}}{100 \exp\left(\frac{A}{D(RH_{dry})}\right) - RH_{dry}} - \frac{RH}{100 \exp\left(\frac{A}{D(RH)}\right) - RH} \right] \quad (12)$$

The derivation of Eq. 12 is provided in Supplementary Method. By utilizing the median diameters (D_{median}) of the dry and wet PNSDs measured by two SMPS, $g(RH)$ and subsequently the related κ, κ_g, can be calculated.

The hygroscopic growth factor for light scattering ($f(RH)$) is defined as the ratio of σ_{sc} at a specific RH to the corresponding dry σ_{sc}, expressed as:

$$f(RH) = \frac{\sigma_{sc}(RH)}{\sigma_{sc}(RH_{dry})} \quad (13)$$

In this study, σ_{sc} at 525 nm was used to calculate f(RH). Based on the κ-Köhler equation, Brock et al.[74] introduced a single-parameter representation to characterize $f(RH)$, and Kuang et al.[67] extended this by considering that RH_{dry} is not zero in dry nephelometer, leading to the following formulation:

$$f(RH) = \left(1 + \kappa_{sc} \frac{RH}{100 - RH}\right) \Big/ \left(1 + \kappa_{sc} \frac{RH_{dry}}{100 - RH_{dry}}\right) \quad (14)$$

where κ_{sc} is a parameter that best fits the $f(RH)$ relationship. It is worth noting that the assumed linearly positive relationship between V_a and σ_{sc} results in κ_{sc} not entirely conforming to the conventional interpretation of aerosol κ. To address this, Kuang et al.[67] introduced a method for calculating the overall aerosol κ derived from measured $f(RH)$, denoted as κ_f. κ_f is influenced by κ_{sc} and the Ångström exponent. The Ångström exponent can be determined using σ_{sc} values at 450 nm and 525 nm measured by the dry nephelometer in PB-FRH100. Subsequently, κ_f can be calculated. Note that the calculation of κ_{sc} in Eq. 14 does not account for the curvature effect, introducing slight bias in the subsequent calculating κ_f.

Additionally, the total V_a can be calculated by assuming spherical particles. The hygroscopic growth factor for V_a ($V(RH)$) is defined as the ratio of wet V_a at a specific RH to the corresponding dry V_a, expressed as:

$$V(RH) = \frac{V_a(RH)}{V_a(RH_{dry})} \quad (15)$$

In a similar manner to Eq. 14, volume-weighted mean κ, κ_v, is calculated using $V(RH)$ as

$$V(RH) = \left(1 + \kappa_v \frac{RH}{100 - RH}\right) \Big/ \left(1 + \kappa_v \frac{RH_{dry}}{100 - RH_{dry}}\right) \quad (16)$$

It is crucial to emphasize that the RH output from the SMPS pertains to the RH of the sheath gas that has passed through the heat exchanger, rather than the RH of the sample gas. In this study, we relied on the RH obtained from the automated weather station (WXT530, Vaisala Inc.) as the ambient RH, and the RH measured in the dry nephelometer of PB-FRH100 as the RH_{dry}. It should be noted that there are deviations between the ambient RH and the RH of the wet sample gas. During clouds (fogs) formation, water accumulates in the storage bottle, resulting in both the ambient RH and the RH at the inlet of the wet SMPS being high, with little disparity between them. However, in the absence of clouds (fogs) and no water accumulation in the bottle, the ambient RH may be slightly higher than the wet SMPS inlet RH due to moisture loss in the sample gas pipeline. These deviations in RH can lead to deviations in the calculation results of κ_v and κ_g. As shown in Supplementary Fig. 9, a 10% increase or decrease in the absolute value of the sample gas RH leads to a respective halving or doubling of κ_v (and κ_g). Assuming a deviation of ±10% between the RH at the wet SMPS inlet and the ambient RH, the mean range for κ_v is 0.015 to 0.099, and for κ_g is 0.025 to 0.122, still indicating weak hygroscopicity. For future experiments, it is advisable to install a hygrometer between the water storage bottle and the wet SMPS inlet to precisely measure the RH of the wet sample gas, thereby mitigating biases in κ_v and κ_g calculations.

HYSPLIT model

Utilizing three-day backward trajectories generated by the HYSPLIT model[75] (https://www.arl.noaa.gov/hysplit/, last access: 30 October 2023), we calculated a total of 1464 trajectories throughout the experimental period. The estimated lifetime of the measured aerosols is approximately 3 days. Consequently, the period for calculating backward trajectories was set to 3 days, a common practice in the majority of aerosol studies conducted in the TP region e.g.,[76,77]. These trajectories were initiated at a height of 100 m and calculated at hourly intervals. Subsequently, we identified three clusters from the 1464 trajectories, as illustrated in Fig. 1. The prevailing air masses predominantly originated from the southern regions with relatively lower altitudes. Roughly two-thirds of the air masses originated from local emissions and short-range transport within a 100-kilometer distance to the southwest (C1). Air masses from the southeast, associated with medium-range transport, constituted 31% of the total (C2), while air masses from the southwest, characterized by long-range transport, were the least common, accounting for 4% (C3). Abundant water vapor from the Indian Ocean, lifted by the terrain as the air mass travels northward, frequently results in forming clouds and precipitation at the observation site.

Data availability

The data used in this study are available from https://doi.org/10.6084/m9.figshare.24708840.v2.

Code availability

The codes that support the findings of this study are available from Yuan Wang (wang_yuan@lzu.edu.cn) and Jiming Li upon request.

Received: 9 January 2024; Accepted: 19 March 2024;
Published online: 23 March 2024

References

1. Rosenfeld, D. et al. Aerosol-driven droplet concentrations dominate coverage and water of oceanic low-level clouds. *Science* **363**, 6427 (2019).
2. Zhao, C. et al. Aerosol first indirect effects on non-precipitating low-level liquid cloud properties as simulated by CAM5 at ARM sites. *Geophys. Res. Lett.* **39**, L08806 (2012).
3. Fan, J. et al. Substantial convection and precipitation enhancements by ultrafine aerosol particles. *Science* **359**, 411–418 (2018).
4. Wang, Y. et al. Long-term impacts of aerosols on precipitation and lightning over the Pearl River Delta megacity area in China. *Atmos. Chem. Phys.* **11**, 12421–12436 (2011).
5. Twomey, S. Pollution and the planetary albedo. *Atmos. Environ.* **8**, 1251–1256 (1974).
6. Twomey, S. The influence of pollution on the shortwave albedo of clouds. *J. Atmos. Sci.* **34**, 1149–1152 (1977).
7. Zhao, C. F. & Garrett, T. J. Effects of Arctic haze on surface cloud radiative forcing. *Geophys. Res. Lett.* **42**, 557–564 (2015).
8. Che, H. et al. Aerosol optical and radiative properties and their environmental effects in China: a review. *Earth Sci. Rev.* **248**, 104634 (2023).
9. Ramanathan, V., Crutzen, P. J., Kiehl, J. T. & Rosenfeld, D. Aerosols, climate, and the hydrological cycle. *Science* **294**, 2119–2124 (2001).
10. Bellouin, N. et al. Bounding global aerosol radiative forcing of climate change. *Rev. Geophys.* **58**, e2019RG000660 (2020).

11. IPCC, 2021. In Climate Change 2021, the Physical Science Basis (eds. Masson-Delmotte, V. et al.) 959 (Cambridge University Press, 2021).
12. Gantt, B., He, J., Zhang, X., Zhang, Y. & Nenes, A. Incorporation of advanced aerosol activation treatments into CESM/CAM5: model evaluation and impacts on aerosol indirect effects. *Atmos. Chem. Phys.* **14**, 7485–7497 (2014).
13. Seinfeld, J. H. et al. Improving our fundamental understanding of the role of aerosol-cloud interactions in the climate system. *Proc. Natl Acad. Sci. USA* **113**, 5781–5790 (2016).
14. Köhler, H. The nucleus in and the growth of hygroscopic droplets. *Trans. Farad. Soc.* **32**, 1152–1161 (1936).
15. Twomey, S. The nuclei of natural cloud formation part II: the supersaturation in natural clouds and the variation of cloud droplet concentration. *Geofisica Pura Applicata* **43**, 243–249 (1959).
16. Petters, M. D. & Kreidenweis, S. M. A single parameter representation of hygroscopic growth and cloud condensation nuclei activity. *Atmos. Chem. Phys.* **7**, 1961–1971 (2007).
17. Mikhailov, E., Vlasenko, S., Rose, D. & Pöschl, U. Mass-based hygroscopicity parameter interaction model and measurement of atmospheric aerosol water uptake. *Atmos. Chem. Phys.* **13**, 717–740 (2013).
18. Paramonov, M. et al. A synthesis of cloud condensation nuclei counter (CCNC) measurements within the EUCAARI network. *Atmos. Chem. Phys.* **15**, 12211–12229 (2015).
19. Pöhlker, M. L. et al. Global organic and inorganic aerosol hygroscopicity and its effect on radiative forcing. *Nat. Commun.* **14**, 6139 (2023).
20. Gunthe, S. S. et al. Cloud condensation nuclei in pristine tropical rainforest air of Amazonia: size-resolved measurements and modeling of atmospheric aerosol composition and CCN activity. *Atmos. Chem. Phys.* **9**, 7551–7575 (2009).
21. Pöhlker, M. L. et al. Long-term observations of cloud condensation nuclei in the Amazon rain forest – Part 1: aerosol size distribution, hygroscopicity, and new model parametrizations for CCN prediction. *Atmos. Chem. Phys.* **16**, 15709–15740 (2016).
22. Rose, D. et al. Cloud condensation nuclei in polluted air and biomass burning smoke near the mega-city Guangzhou, China – Part 1: size-resolved measurements and implications for the modeling of aerosol particle hygroscopicity and CCN activity. *Atmos. Chem. Phys.* **10**, 3365–3383 (2010).
23. Salma, I., Thén, W., Vörösmarty, M. & Gyöngyösi, A. Z. Cloud activation properties of aerosol particles in a continental Central European urban environment. *Atmos. Chem. Phys.* **21**, 11289–11302 (2021).
24. Chen, L. et al. Hygroscopic growth of ambient fine particles measured at five sites in China. *Atmos. Chem. Phys.* **22**, 6773–6786 (2022).
25. Wu, Z. et al. Particle hygroscopicity and its link to chemical composition in the urban atmosphere of Beijing, China, during summertime. *Atmos. Chem. Phys.* **16**, 1123–1138 (2016).
26. Fors, E. O. et al. Hygroscopic properties of the ambient aerosol in southern Sweden – a two-year study. *Atmos. Chem. Phys.* **11**, 8343–8361 (2011).
27. Wang, Y. et al. Aerosol activation characteristics and prediction at the central European ACTRIS research station of Melpitz, Germany. *Atmos. Chem. Phys.* **22**, 15943–15962 (2022).
28. Kristensen, T. B. et al. Properties of cloud condensation nuclei (CCN) in the trade wind marine boundary layer of the western North Atlantic. *Atmos. Chem. Phys.* **16**, 2675–2688 (2016).
29. Bougiatioti, A. et al. Biomass-burning impact on CCN number, hygroscopicity and cloud formation during summertime in the eastern Mediterranean. *Atmos. Chem. Phys.* **16**, 7389–7409 (2016).
30. Henning, S. et al. Influence of cloud processing on CCN activation behaviour in the Thuringian Forest, Germany during HCCT-2010. *Atmos. Chem. Phys.* **14**, 7859–7868 (2014).
31. Schmale, J. et al. Long-term cloud condensation nuclei number concentration, particle number size distribution and chemical composition measurements at regionally representative observatories. *Atmos. Chem. Phys.* **18**, 2853–2881 (2018).
32. Andreae, M. O. & Rosenfeld, D. Aerosol-cloud-precipitation interactions, Part 1, the nature and sources of cloud-active particles. *Earth-Sci. Rev.* **89**, 13–41 (2008).
33. Pringle, K. J., Tost, H., Pozzer, A., Pöschl, U. & Lelieveld, J. Global distribution of the effective aerosol hygroscopicity parameter for CCN activation. *Atmos. Chem. Phys.* **10**, 5241–5255 (2010).
34. Kerminen, V.-M. et al. Cloud condensation nuclei production associated with atmospheric nucleation: a synthesis based on existing literature and new results. *Atmos. Chem. Phys.* **12**, 12037–12059 (2012).
35. Wang, Y. et al. Characterization of aerosol hygroscopicity, mixing state, and CCN activity at a suburban site in the central North China Plain. *Atmos. Chem. Phys.* **18**, 11739–11752 (2018).
36. Schulze, B. C. et al. Characterization of aerosol hygroscopicity over the Northeast Pacific Ocean: impacts on prediction of CCN and stratocumulus cloud droplet number concentrations. *Earth Sp. Sci.* **7**, 001098 (2020).
37. Kang, S. et al. Review of climate and cryospheric change in the Tibetan Plateau. *Environ. Res. Lett.* **5**, 1–8 (2010).
38. Liu, Y. et al. Aerosol-cloud interactions over the Tibetan Plateau: an overview. *Earth-Sci. Rev.* **234**, 104216 (2022).
39. Xu, J. et al. High-resolution physicochemical dataset of atmospheric aerosols over the Tibetan Plateau and its surroundings. *Earth Syst. Sci. Data Discuss*. [preprint], https://doi.org/10.5194/essd-2023-506 (2023).
40. Zhou, X. et al. Aerosol effects on the development of cumulus clouds over the Tibetan Plateau. *Atmos. Chem. Phys.* **17**, 7423–7434 (2017).
41. Fu, Y. et al. Land-surface processes and summer-cloud-precipitation characteristics in the Tibetan Plateau and their effects on downstream weather: a review and perspective. *Natl Sci. Rev.* **7**, 500–515 (2020).
42. Xu, X. et al. Effects of cloud liquid-phase microphysical processes in mixed-phase cumuli over the Tibetan Plateau. *J. Geophys. Res. Atmos.* **125**, D033371 (2020).
43. Li, J. et al. The influence of complex terrain on cloud and precipitation on the foot and slope of the southeastern Tibetan Plateau. Clim. Dyn. (2024).
44. Zhao, Y., Li, J., Zhang, W., Deng, C. & Li, Y. Cloud response is significantly biased by CMIP6 over the Tibetan Plateau. *Geophys. Res. Lett.* **49**, L100903 (2022).
45. Zhao, Y. et al. Diurnal cycles of cloud cover and its vertical distribution over the Tibetan Plateau revealed by satellite observations, reanalysis datasets, and CMIP6 outputs. *Atmos. Chem. Phys.* **23**, 743–769 (2023).
46. Wang, Y. et al. A new method for distinguishing unactivated particles in cloud condensation nuclei measurements: implications for aerosol indirect effect evaluation. *Geophys. Res. Lett.* **46**, 14185–14194 (2019).
47. Wang, Y. et al. A new CCN activation parameterization and its potential Influences on Aerosol indirect effects. *Atmos. Res.* **253**, 105491 (2021).
48. Kim, J. H. et al. On the submicron aerosol distributions and CCN number concentrations in and around the Korean Peninsula. *Atmos. Chem. Phys.* **14**, 8763–8779 (2014).
49. Seinfeld, J. H. & Pandis, S. N. Atmospheric Chemistry and Physics: From Air Pollution to Climate Change 731 (John Wiley & Sons, Inc. Hoboken, 2016).
50. Wu, Z. J. et al. Relating particle hygroscopicity and CCN activity to chemical composition during the HCCT-2010 field campaign. *Atmos. Chem. Phys.* **13**, 7983–7996 (2013).
51. Cai, M. et al. The size-resolved cloud condensation nuclei (CCN) activity and its prediction based on aerosol hygroscopicity and composition in the Pearl Delta River (PRD) region during wintertime 2014. *Atmos. Chem. Phys.* **18**, 16419–16437 (2018).

52. Zhao, P. S., Ge, S. S., Su, J., Ding, J. & Kuang, Y. Relative humidity dependence of hygroscopicity parameter of ambient aerosols. *J. Geophys. Res. Atmos.* **127**, e2021JD035647 (2022).
53. Wang, L. et al. Investigation of biogenic volatile organic compounds emissions in the Qinghai-Tibetan Plateau. *Sci. Total Environ.* **902**, 165877 (2023).
54. Prenni, A. J., Petters, M. D., Kreidenweis, S. M., DeMott, P. J. & Ziemann, P. J. Cloud droplet activation of secondary organic aerosol. *J. Geophys. Res.* **112**, D10223 (2007).
55. Zhang, X., Xu, J., Zhai, L. & Zhao, W. Characterization of aerosol properties from the burning emissions of typical residential fuels on the Tibetan Plateau. *Environ. Sci. Technol.* **56**, 14296–14305 (2022).
56. Shen, C., Zhao, G., Zhao, W., Tian, P. & Zhao, C. Measurement report: aerosol hygroscopic properties extended to 600 nm in the urban environment. *Atmos. Chem. Phys.* **21**, 1375–1388 (2021).
57. Dusek, U. et al. Size matters more than chemistry for cloud-nucleating ability of aerosol particles. *Science* **312**, 1375–1378 (2006).
58. Stephens, G. L. The parameterization of radiation for numerical weather predication and climate models. *Mon. Wea. Rev.* **112**, 826–867 (1984).
59. Liu, Y. & Daum, P. H., Anthropogenic aerosols. Indirect warming effect from dispersion forcing. *Nature* **419**, 580 (2002).
60. Quaas, J., Boucher, O. & Bréon, F. M. Aerosol indirect effects in POLDER satellite data and the Laboratoire de Météorologie Dynamique Zoom (LMDZ) general circulation model. *J. Geophys. Res.* **109**, D08205 (2004).
61. Liu, Y., Daum, P. H., McGraw, R. & Miller, M. Generalized threshold function accounting for effect of relative dispersion on threshold behavior of autoconversion process. *Geophys. Res. Lett.* **33**, L11804 (2006).
62. Liu, Y., Daum, P. H. & McGraw, R. An analytical expression for predicting the critical radius in the autoconversion parameterization. *Geophys. Res. Lett.* **31**, L06121 (2004).
63. Ditas, F. et al. Aerosols-cloud microphysics-thermodynamics-turbulence: evaluating supersaturation in a marine stratocumulus cloud. *Atmos. Chem. Phys.* **12**, 2459–2468 (2012).
64. Mazoyer, M. et al. Experimental study of the aerosol impact on fog microphysics. *Atmos. Chem. Phys.* **19**, 4323–4344 (2019).
65. Wang, Y. et al. Observational study of the physical and chemical characteristics of the winter radiation fog in the tropical rainforest in Xishuangbanna. *China Sci. China Earth Sci.* **64**, 1982–1995 (2021).
66. Tian, P. et al. Atmospheric aerosol size distribution impacts radiative effects over the Himalayas via modulating aerosol single-scattering albedo. *npj Clim. Atmos. Sci.* **6**, 54 (2023).
67. Kuang, Y. et al. A novel method for deriving the aerosol hygroscopicity parameter based only on measurements from a humidified nephelometer system. *Atmos. Chem. Phys.* **17**, 6651–6662 (2017).
68. Zhao, P. S., Ding, J., Du, X. & Su, J. High time-resolution measurement of light scattering hygroscopic growth factor in Beijing: a novel method for high relative humidity conditions. *Atmos. Environ.* **215**, 116912 (2019).
69. Rose, D. et al. Calibration and measurement uncertainties of a continuous-flow cloud condensation nuclei counter (DMT-CCNC): CCN activation of ammonium sulfate and sodium chloride aerosol particles in theory and experiment. *Atmos. Chem. Phys.* **8**, 1153–1179 (2008).
70. Vepsäläinen, S., Calderón, S. M., Malila, J. & Prisle, N. L. Comparison of six approaches to predicting droplet activation of surface active aerosol – Part 1: moderately surface active organics. *Atmos. Chem. Phys.* **22**, 2669–2687 (2022).
71. Sihto, S.-L. et al. Seasonal variation of CCN concentrations and aerosol activation properties in boreal forest. *Atmos. Chem. Phys.* **11**, 13269–13285 (2011).
72. Tao, J. et al. Kinetic limitations affect cloud condensation nuclei activity measurements under low supersaturation. *Geophys. Res. Lett.* **50**, 1–9 (2023).
73. Raatikainen, T., Moore, R. H., Lathem, T. L. & Nenes, A. A coupled observation – modeling approach for studying activation kinetics from measurements of CCN activity. *Atmos. Chem. Phys.* **12**, 4227–4243 (2012).
74. Brock, C. A. et al. Aerosol optical properties in the southeastern United States in summer – Part 1: Hygroscopic growth. *Atmos. Chem. Phys.* **16**, 4987–5007 (2016).
75. Stein, A. F. et al. NOAA's HYSPLIT atmospheric transport and dispersion modeling system. *Bull. Am. Meteor. Soc.* **96**, 2059–2077 (2015).
76. Xu, J. et al. Chemical characteristics of submicron particles at the central Tibetan Plateau: insights from aerosol mass spectrometry. *Atmos. Chem. Phys.* **18**, 427–443 (2018).
77. Zhang, L. et al. Unexpected high absorption of atmospheric aerosols over a Western Tibetan Plateau site in summer. *J. Geophys. Res. Atmos.* **126**, e2020JD033286 (2021).

Acknowledgements

This research is supported by the Second Tibetan Plateau Scientific Expedition and Research Program (STEP) under Grant No. 2019QZKK0602, the National Natural Science Foundation of China under Grant No. 42205072, and the Science and Technology Planning Project of Gansu Province under Grant No. 22JR5RA445. We thank Tao Wang and Hao Zhang for the careful maintenance of the measurements on-site.

Author contributions

Yuan Wang, J.L. and Jianping Huang designed the study and received the funding. Yuan Wang, J.L., F.F. and P.Z. analyzed the data and led the writing. Yuan Wang and J.S. conducted the field campaigns. All authors contributed to the discussion, review, and editing.

Competing interests

The authors declare no competing interests.

Additional information

Supplementary information The online version contains supplementary material available at https://doi.org/10.1038/s41612-024-00629-x.

Correspondence and requests for materials should be addressed to Jiming Li.